AIP Journal of Applied Physics

Electronic transport properties of graphene channel with metal electrodes or insulating substrates in 10 nm-scale devices

H. Jippo, T. Ozaki, S. Okada, and M. Ohfuchi

Citation: Journal of Applied Physics **120**, 154301 (2016); doi: 10.1063/1.4964948
View online: http://dx.doi.org/10.1063/1.4964948
View Table of Contents: http://scitation.aip.org/content/aip/journal/jap/120/15?ver=pdfcov
Published by the AIP Publishing

Electronic transport properties of graphene channel with metal electrodes or insulating substrates in 10 nm-scale devices

H. Jippo,[1] T. Ozaki,[2] S. Okada,[3] and M. Ohfuchi[1]
[1]*Fujitsu Laboratories Ltd., Atsugi, Kanagawa 243-0197, Japan*
[2]*Institute for Solid State Physics, The University of Tokyo, Kashiwa 277-8581, Japan*
[3]*Graduate School of Pure and Applied Sciences, University of Tsukuba, 1-1-1 Tennodai, Tsukuba, Ibaraki 305-8571, Japan*

(Received 20 July 2016; accepted 5 October 2016; published online 18 October 2016)

We have studied the electronic transport properties of armchair graphene nanoribbons (AGNRs) bridged between two metal electrodes or supported on insulating substrates in 10 nm-scale devices using the first-principles calculations. The two metal species of Ti and Au are examined as metal electrodes and are compared. The current densities through the AGNR-Ti contact are about 10 times greater than those through the AGNR-Au contact, even though the AGNR width reaches 12 nm. For the insulating substrates, we have investigated the dependence of the channel length on the transport properties using models with two channel lengths of 15.1 and 9.91 nm. Regardless of the channel length, the on/off current ratio is 10^5 for the AGNRs on an O-terminated surface. This ratio is consistent with the recent experiments and is less by factors of 10^{16} for the 15.1 nm channel length and 10^8 for the 9.91 nm channel length compared to the freestanding AGNR. *Published by AIP Publishing.*
[http://dx.doi.org/10.1063/1.4964948]

I. INTRODUCTION

Graphene has been extensively studied for use in nanoelectronics because of its unique electronic and geometric properties. A honeycomb network with one-atom thickness leads to massless electrons and holes around the Fermi level. The high carrier mobility allows the material to be applied to the high-speed electronic devices in the post-silicon era. On the other hand, the electronic properties of graphene are significantly fragile against the surrounding foreign materials, such as metal electrodes[1–14] and insulating substrates.[15–26] This is because the whole area of graphene intrinsically forms interfaces with such foreign materials. The fragility of the electronic properties will constitute a serious problem for designing the graphene-based electronic devices especially in the 10 nm-scale, which is considered for future realization when graphene devices can potentially be used in practice.

Graphene contacted with metal electrodes has already studied intensely. In addition to high contact resistance, it has been experimentally reported that the resistance also depends on the metal species.[1–6] Wide variations have also been found in contact resistance even within the same species. Several theoretical studies reported geometries, electronic structures of interfaces between graphene and metal surfaces.[7,8,10] The transport properties have also been studied actively.[11–14] It was found that the contact resistance of the Ni-graphene system is one order of magnitude lower than that of Cu-graphene for graphene channels of a few nm in length.[12] We previously reported that currents sensitively depend on the width of armchair graphene nanoribbons (AGNRs) up to 12 nm for the Au-graphene hybrid structures using the first-principles electronic transport calculations.[14] However, the dependence of the transport properties on metal species has not yet been ascertained for AGNRs over 10 nm in width.

Graphene on the insulating substrates is another active area of research. Experiments have shown degradation of the carrier mobility and the on/off current ratio for graphene adsorbed on SiO_2.[15–17,19,20] The surface treatment of SiO_2 even changes the electronic transport properties of graphene. The primary structures of silica surfaces are known to be siloxane groups (Si–O–Si) and silanol groups (Si–OH).[27] Silanol groups on the SiO_2 surface degrade the mobility and shift the Dirac point of graphene.[18] From a theoretical perspective, several studies on the geometrical and electronic properties of graphene on SiO_2 have been reported using the first-principles methods.[21–25] Regarding the electronic transport properties, we previously reported on the first-principles study of AGNRs with the channel length $L = 9.91$ nm on O- and OH-terminated SiO_2/Si surfaces.[26] The on/off current ratio for AGNRs on both the surfaces is less than that of the freestanding (FS) AGNR. However, more comprehensive research is necessary to understand the dependence of channel length on the transport properties.

In this paper, we aim to give a theoretical insight into the electronic transport properties at the interface between graphene and foreign materials in terms of realization of 10 nm-scale devices. We first look at the electronic transport properties of AGNRs bridged between the two Ti electrodes using the first-principles calculations. The results are compared with our previous data for Au electrodes[14] in order to examine the dependence of the transport properties on metal species. Next, we study the dependence of channel length on the electronic transport properties of AGNRs on SiO_2/Si using the first-principles calculations. Models with a channel length of $L = 15.1$ nm are compared with those for $L = 9.91$ nm in our previous paper. Some supplemental data for $L = 9.91$ nm are also presented.

II. METHODS

A. Computational details

For all calculations, we employ the density functional theory (DFT) code OpenMX,[28,29] which enables us to realize large-scale calculations on massively parallel computers.[30,31] The exchange-correlation potential is treated with a generalized gradient approximation (GGA) using the Perdew–Burke–Ernzerhof (PBE) functional.[32] The electron-ion interaction is described by norm-conserving pseudopotentials[33] with a partial core correction.[34] Pseudo-atomic orbitals (PAOs) centered on atomic sites are used as the basis function set.[28]

For geometrical optimizations, we use the PAOs specified by C6.0-*s*2*p*2*d*1, H5.0-*s*2*p*1, Ti7.0-*s*3*p*3*d*2, and Au7.0-*s*2*p*2*d*2*f*1 for the graphene-metal hybrid structures and C7.0-*s*2*p*2*d*1, H7.0-*s*2*p*1, Si7.0-*s*2*p*2*d*1, and O7.0-*s*2*p*2*d*1 for the graphene-SiO_2/Si hybrid structures. For example, C6.0-*s*2*p*2*d*1 indicates the PAO of the carbon atom with the cutoff radii of 6.0 bohr and with the following components: two *s*, two *p*, and one *d*. The real-space grid techniques are used with a grid cell length of $l_g = 0.13$ bohr in the numerical integrations and the solution of Poisson's equation using the fast Fourier transform. For the graphene-SiO_2/Si hybrid structure, we also use the O(*N*) scheme based on the Krylov subspace methods implemented in OpenMX.[35] The radius of truncated clusters and the dimension of the Krylov subspace are set at 1.1 nm and 1500, respectively. Geometries are optimized under a three-dimensional periodic boundary condition, and the convergence criterion for forces on atoms is set at 0.1 eV/nm.

For transport calculations, we employ the non-equilibrium Green's function (NEGF) method implemented in OpenMX[29] to calculate the electronic structures. We use a smaller set of PAOs, i.e., C-*s*1*p*2, H-*s*1, Ti-*s*1*p*2*d*1, Au-*s*1*p*2*d*1, Si-*s*1*p*1, and O-*s*1*p*1, and a larger grid cell length $l_g = 0.30$ bohr, in order to reduce the computational cost. The cutoff radii of the PAOs are the same as those for the geometrical optimizations.

B. Accuracy checks in the transport calculations

We first discuss the validity of using the small basis set in the transport calculations. Figure S1 in the supplementary material shows the comparison of the energy band structures of graphene on an Au(111) surface modeled by the slab with four layers using the small basis set of PAOs (red lines) and the large set of PAOs (green lines). We can find little difference between the band structures using the two PAO sets. The energy of the Dirac point in graphene at the *K* point is 0.34 eV for the small set and 0.37 eV for the large set. The difference in the Fermi velocity of the graphene's bands around the Dirac point is within 5% between the small and large basis sets. This may cause 5% error in the current of the models for graphene bridging metal electrodes.

We also make a small unit cell model with graphene on SiO_2/Si as shown in Fig. S2(a) in the supplementary material. The graphene is compressed by 11% along the *x*-direction and expanded by 4% along the *y*-direction to match with the lateral unit cell of SiO_2/Si. Figures S2(b) and S2(c) show the energy band structures of the model obtained using the large and small basis sets, respectively. Both the basis sets give a zero gap at the Dirac point. The Dirac point in the compressed graphene is shifted to the Γ-Y direction from the Γ-point, where the K-point is folded under the equilibrium lattice constant. The energy of the Dirac point in graphene is 0.25 eV for the small set and 0.16 eV for the large set. The Fermi velocities are different by 6% between the two basis sets.

The accuracy of the large grid cell length ($l_g = 0.30$ bohr) in the transport calculations is next examined using the short-channel model with a channel length of 0.86 nm, as shown in Fig. S3(a) in the supplementary material. The model is composed of two units of the AGNR channel with a number of C_2 dimer rows, $N = 7$, sandwiched between the semi-infinite leads. For simplicity, the leads were made of AGNRs with $N = 8$ under a uniaxial expansion of 1.86% along the *x*-direction from the configuration of the graphene sheet for use as an artificial metal. The strain changes the electronic property of AGNRs from semiconducting to metallic.[36,37] We calculated the current densities for the model at two bias voltages of 0.5 V and 1.0 V using the NEGF method. The errors in the current densities are shown in Fig. S3(b). The obtained current density for $l_g = 0.30$ bohr is less than 3% below that for $l_g = 0.13$ bohr, which is the value employed in the geometric optimization.

We concluded that the small set of PAOs and the large grid cell length $l_g = 0.30$ bohr are adequate to discuss the transport properties of AGNRs on foreign materials. These treatments make a significant contribution to reduce the computational cost.

III. GRAPHENE/METAL ELECTRODES

A. Interfaces

The interface between graphene and metals is simulated by the repeated slab model consisting of a single graphene sheet and four atomic layers of metals. Figures S4(a) and S4(b) in the supplementary material show the optimized structures of graphene adsorbed on Ti(0001) and Au(111) surfaces, respectively. Although the Au(111) surface was described in Ref. 14, the results are presented again in this paper for comparison. One carbon atom is situated above the topmost metal atom, and the other is on a bridge site for both the metal surfaces.[7] The lattice constant of graphene is 2.47 Å. A commensurability condition is imposed between the lateral periodicities of graphene and that of the metal surfaces. Accordingly, the rectangular unit cell contains the $2 \times 2\sqrt{3}$ lateral periodicity of graphene and the $\sqrt{3} \times 3$ lateral periodicity of the Ti(0001) and Au(111) surfaces. Since there are lattice mismatches between graphene and metal surfaces, the lateral lattice parameter of the Ti(0001) and Au(111) surfaces is compressed by 2.65% and 3.23% from the equilibrium lattice parameter, respectively. The electronic structures of AGNRs are sensitive to the structural deformations.[36] Therefore, we here deform only the metal surfaces for the purpose of investigating the ideal transport properties of graphene itself depending on the contacting metals. The artificial lattice compression causes a slight change in the

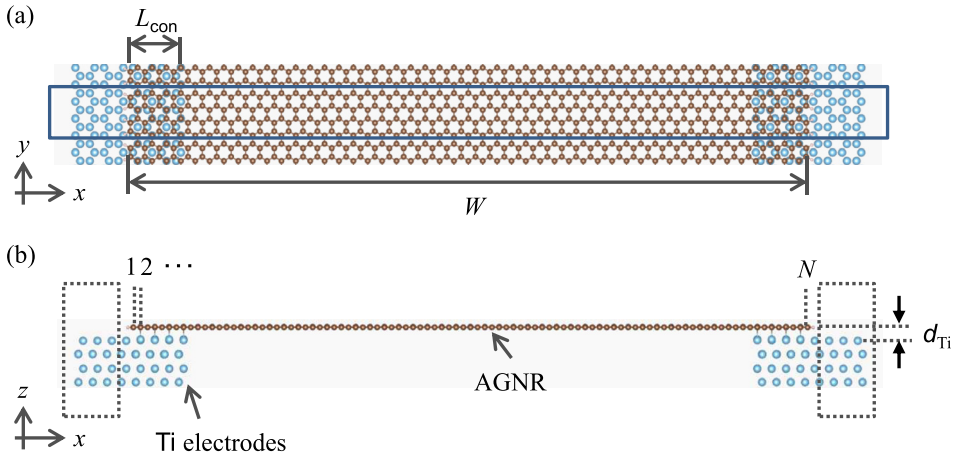

FIG. 1. (a) Top and (b) side views of the structural model for the first-principles electronic transport calculations based on the non-equilibrium Green's function (NEGF) method. The armchair graphene nanoribbon (AGNR) with the number of C_2 dimer rows $N = 95$, where the ribbon width $W = 11.6$ nm, is bridged between left and right Ti electrodes with the contact length $L_{con} = 0.86$ nm. The armchair edges located on the Ti electrodes are terminated by the hydrogen atoms represented by the white spheres. The solid rectangle in (a) indicates the unit cell of the model. The dashed rectangles in (b) indicate the unit cells of leads. The interlayer spacing d_{Ti} is set to 0.20–0.22 nm. Although both sides in the transport direction (x) are connected to semi-infinite leads in actual calculations, only atoms of the center region are given.

work function from 4.42 eV to 4.53 eV for the Ti(0001) surface and from 5.33 eV to 5.36 eV for the Au(111) surface, where the work function is evaluated as the difference between the Hartree potential in the vacuum and the Fermi energy by placing empty atoms on the metal surfaces.

The equilibrium spacing between graphene and the topmost metal atom is found to be $d_{Ti} = 0.20$–0.22 nm for the Ti(0001) surface and $d_{Au} = 0.37$ nm for the Au(111) surface. The binding energy is calculated using $E_b = E(\mathrm{G/M}) - \{E(\mathrm{G}) + E(\mathrm{M})\}$, where $E(\mathrm{G/M})$, $E(\mathrm{G})$, and $E(\mathrm{M})$ are the total energies of the graphene on the metal, the isolated graphene, and the isolated metal, respectively. Calculated energies E_b are 0.312 eV/carbon atom on the Ti(0001) surface and 0.016 eV/carbon atom on the Au(111) surface. These results of the spacing and the binding energy indicate that graphene is strongly and weakly bound to the Ti(0001) and the Au(111) surface, respectively.

Figure S5 in the supplementary material shows the projected density of states (PDOS) of a p_z orbital of a C atom in graphene and d-z^2 orbital of a topmost metal atom for the (a) Ti(0001) and (b) Au(111) surfaces. The electronic states of the graphene are dramatically modulated by the strong π-d hybridization on the Ti(0001) surface, whose d states are located around the Fermi level E_F. However, the shape of the PDOS of isolated graphene is almost kept due to the weak hybridization on the Au(111) surface, whose d states are located far below the E_F. The energy is shifted upwards by 0.37 eV, indicating the p-type doping from the Au(111) surface. The amount of hybridization is determined by the energy location of metal d states with respect to the E_F.

B. Transport properties

Figure 1 shows a structural model for simulating the transport properties of the hybrid structure that consists of an AGNR and Ti electrodes. Similar models were used for the AGNR/Au hybrid structures. The AGNRs with a width $W \sim 12$ nm are bridged between the two Ti electrodes with the contact length $L_{con} = 0.86$ nm. All the edge carbon atoms along the y direction are terminated by hydrogen atoms, and the armchair edges appear in the contact region. Along the y direction, we impose the periodic boundary condition. N is defined as the number of C_2 dimer rows along the ribbon direction (x direction). Both sides of the unit cell in the x direction are connected to semi-infinite leads. The relaxed geometry of graphene on the four-layer slab of the Ti(0001) and Au(111) surfaces is used as the geometry of the contact region.

Table I shows the current densities I_{Ti} and I_{Au} for the models of the AGNR bridged between Ti and Au electrodes, respectively. The current densities are calculated without a gate voltage. A bias voltage of $V_b = (\mu_L - \mu_R)/e = 0.1$ V, where μ_L (μ_R) is a chemical potential of the left (right) electrode, is employed for the assumption of low energy consumption devices in the future. We find that the currents between graphene and metal electrodes depend decisively on the metal species. The I_{Ti} is between 10 and 20 times larger than the I_{Au} even for a width $W \sim 12$ nm, while the I_{Ti} is about 50 times as large as the I_{Au} for the AGNR with $W = 2.71$ nm. We also find that the current densities still depend on the N-families ($N = 3m$, $3m + 1$, and $3m + 2$) of AGNRs even with a width $W \sim 12$ nm.

To ascertain the metal dependence observed in the current densities, we analyze transmission spectra $T(k_y, E)$ as functions of both wave number along the ribbon k_y and energy E. The current density I is calculated using

TABLE I. Current densities I_{Ti} and I_{Au} for the models of the AGNR with the number of C_2 dimer rows N and the width W bridged between Ti and Au electrodes, respectively. The bias voltage is set to $V_b = 0.1$ V.

N	99	97	95	23
W (nm)	12.10	11.85	11.60	2.71
I_{Ti} (A/m)	285	425	302	2362
I_{Au} (A/m)	24	23	30	46

$$I = \frac{1}{L_y}\frac{e}{h}\frac{2}{N_{k_y}}\int_{-\infty}^{\infty}\sum_{k_y} T(k_y, E)[f(E-\mu_L) - f(E-\mu_R)]dE, \tag{1}$$

where N_{ky} (=151) and L_y (=0.86 nm) are the number of k-points and the length of the unit cell of the model along the y direction, respectively. The $T(k_y, E)$ around the energy integration range from $E=0$ to 0.1 eV smeared with the electronic temperature in the Fermi-Dirac function determines the current density at $V_b = 0.1$ V. Figures 2(a) and 2(b) show the transmission spectra $T(k_y, E)$ of the AGNRs with $W = 11.6$ and 2.71 nm, respectively. The transmission for the AGNR with $W = 11.6$ nm bridged between the Ti electrodes occurs at a wide range of k_y and E around the band structure of the isolated AGNR [Fig. 2(c)] due to the strong π-d hybridization. The energy in the transmission spectra is shifted downward by about 0.1 eV, as compared with the band structure of the isolated AGNR, indicating the n-doping from the Ti electrodes. The transmission spectra are seen to have a significantly wide range of k_y and E for the AGNR with $W = 2.71$ nm bridged between the Ti electrodes, where the band character of the isolated AGNR is unclear contrary to that with $W = 11.6$ nm. For the Au electrodes in both W, on the other hand, transmission occurs only at the particular k_y and E at which the electronic energy band emerges in the AGNR. The p-doping from the Au electrodes shifts the energy upward by about 0.15 and 0.37 eV for $W = 11.6$ and 2.71 nm, respectively. We find a large $T(k_y, E)$ within the integration range from $E = 0$ to 0.1 eV for the Ti electrodes in both W, while the transmission is small within the range for the Au electrodes. It follows that the AGNR with the Ti electrodes exhibits larger current densities than those for the AGNR with the Au electrode. The variation of the work function by the deformation of the metal surfaces to the

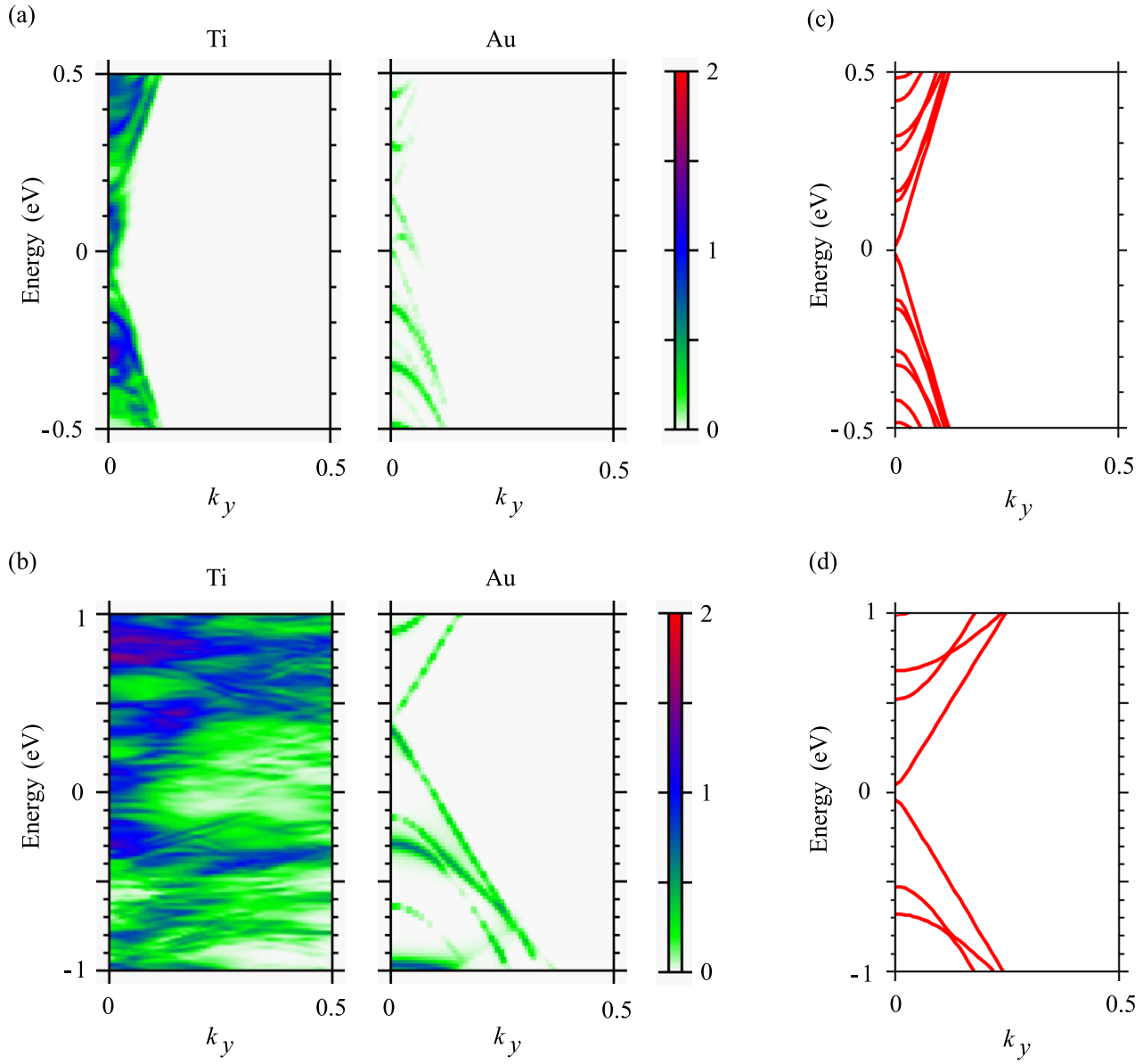

FIG. 2. Transmission spectra $\boldsymbol{T}(\boldsymbol{k_y}, \boldsymbol{E})$ for the AGNR models with (a) $N = 95$ ($W = 11.6$ nm) and (b) $N = 23$ ($W = 2.71$ nm) bridged between the Ti and Au electrodes at a bias voltage $V_b = 0.1$ V. The chemical potentials of the left-side lead $\boldsymbol{\mu_L}$ are set to 0 eV. The right color bar shows the value of $\boldsymbol{T}(\boldsymbol{k_y}, \boldsymbol{E})$. Band structures of the isolated AGNRs with (c) $N = 95$ and (d) $N = 23$.

lattice matching may shift the energy of the transmission spectra by the doping especially for the graphene-Au contact, but the change of the work function of 0.03 eV (from 5.33 eV to 5.36 eV) is smaller than the integration range of 0.1 eV, giving insignificant effect to the current densities.

The W-dependent transmission spectra for the Ti electrode are ascribed to the extent of the recovery of the electronic states of the isolated AGNR. Figure 3 shows PDOS of a C atom at the middle of the AGNR channel with $W = 11.6$ nm and 2.71 nm. The shape of the PDOS for $W = 11.6$ nm is quite similar to that of the isolated AGNR, leading to the transmission spectra reflecting the band character of the isolated AGNR, as shown in Fig. 2(a). However, completely mixed electronic states are found for $W = 2.71$ nm, leading to the wide range transmission spectra, as shown in Fig. 2(b). The larger PDOS around the E_F at the middle of the channel indicates strong hybridization between the whole area of AGNR and the electrode for $W = 2.71$ nm, while the effect of hybridization on the metal contact is decayed and the electronic states of the isolated AGNR are recovered at the middle of the channel for $W = 11.6$ nm, leading to smaller PDOS around the shifted Dirac point at E-$E_F = -0.1$ eV. For the Au electrode, the spectra are relatively independent with the W due to the weak interaction between graphene and the Au(111) surface. The electronic states of the isolated graphene are almost kept even above the Au(111) surface, as shown in Fig. S5(b). The symmetry of the π state of the AGNRs also contributes to reduce the currents with the Au electrodes.[14]

We have found that the currents in the AGNR-Ti contact are over 10 times as great as those in the AGNR-Au contact, even though the AGNR width reaches 12 nm. Nevertheless, the experiment has reported that the Ti contact results in higher contact resistance values ($R_c = 48.0 \pm 5.7$ kΩ μm) compared to the Au contact ($R_c = 3.9 \pm 1.5$ kΩ μm).[5] In this experiment, however, a Ti oxide layer has been observed above the Ti/graphene interface. The oxide layer is considered to act as a barrier layer between the Ti layer and the graphene, resulting in the high R_c. Although we cannot compare directly, in another experiment, the lower R_c of 0.7 ± 0.5 kΩ μm has been performed for the Ti contact by introducing the resist removal process after the graphene etching.[6] The removal of the contamination seems to enhance the π-d hybridization by the direct contact between the Ti surface and the graphene. This experimental result suggests the good potential of the Ti contact, which may be consistent with our result, indicating that the Ti contact is essentially more promising than the Au contact for achieving the low contact resistance.

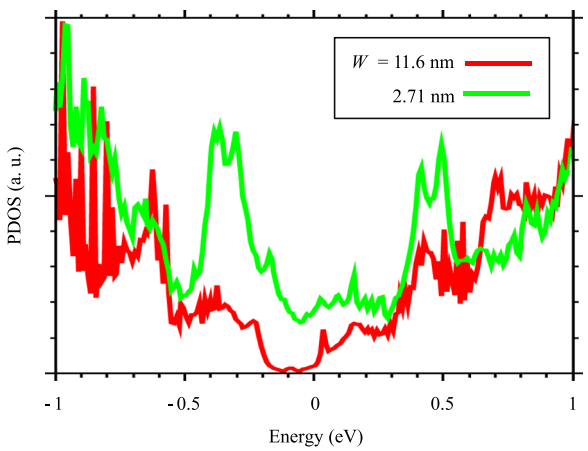

FIG. 3. PDOS of a carbon atom at the middle of the AGNR channel with $W = 11.6$ and 2.71 nm bridged between the two Ti electrodes.

IV. GRAPHENE/INSULATING SUBSTRATES

A. Models

Figure 4 shows a structural model for simulating the transport properties of the hybrid structure of AGNRs on O-terminated SiO_2/Si with the channel length $L = 15.1$ nm. The model with $L = 9.91$ nm in Ref. 26 was almost the same as this model. Note that the transport direction is perpendicular to the ribbon width, contrary to the graphene/metal electrodes model in Sec. III. The channel of an AGNR with $N = 7$ is sandwiched between semi-infinite leads of AGNRs with $N = 8$ under a uniaxial expansion of 1.86% along the x-direction, which were also used as an artificial metal in Sec. II B. All the edge carbon atoms are terminated by hydrogen atoms. The whole geometry of the AGNR channel was optimized using the O(N) method while fixing the atoms in the leads.

The structural model of SiO_2/Si has a fully O-terminated surface without dangling bonds, which was proposed as the most stable surface in the early stages of oxidation of the Si substrate.[38] The two topmost layers of Si are oxidized. The SiO_2 thickness is 0.45 nm, which is also considered as an equivalent oxide thickness (EOT) for the future devices. The model originally had 14 Si layers; however, we extracted six layers and terminated all Si atoms of the bottom layer with hydrogen atoms. We then optimized the geometry by fixing the bottom two Si layers and confirmed that the model maintains the atomic structure with the errors in bond lengths within 1% and the bond angles equal to the original ones. The unit cell of the structure in the xz-plane is indicated by the dotted rectangle in Fig. 4(b), which is also periodic along the y-direction. The end of this structure is cut off on both sides in the x-direction and terminated by hydrogen atoms. The models consist of 13.5 and 8.5 units of the periodic SiO_2/Si structure with $L = 15.1$ and 9.91 nm, respectively. The whole geometry of the SiO_2/Si is also optimized using the O(N) method while fixing the atoms in the bottom two Si layers.

The lateral configuration of the AGNR on SiO_2/Si is randomly selected based on no site selectivity for the graphene/SiO_2 interfaces.[24,25] The geometries of the AGNR and SiO_2/Si are fixed to each optimized structures. We use the spacing of 0.31 nm between the AGNR and SiO_2/Si. The spacing is determined such that the total energy can be minimized in the model with $L = 9.91$ nm in the previous calculation,[26] and it is almost identical to that reported in Refs. 24 and 25.

B. Channel length dependence of transport properties

We investigate the dependence of the transport properties on the channel length. Figure 5 shows the current

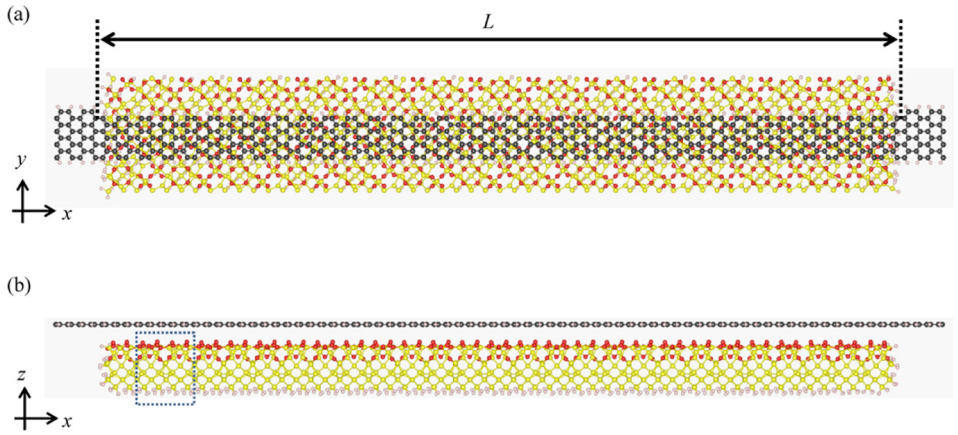

FIG. 4. Model of AGNRs on O-terminated SiO_2/Si used for transport calculations (channel length $L = 15.1$ nm): (a) top and (b) side views. Although both sides in the transport direction (x) are connected to a semi-infinite AGNR in the actual calculations, only atoms in the center region are shown. In the y-direction, only atoms of the unit cell are shown and they are actually repeated periodically. The dotted rectangle in (b) indicates the unit cell of the periodic SiO_2/Si structure. The gray, white, yellow, and red spheres represent carbon, hydrogen, silicon, and oxygen atoms, respectively. The number of atoms in the unit cell amounts to 3030.

densities for the freestanding AGNR and the AGNRs on O- and OH-terminated SiO_2/Si with the channel lengths $L = 15.1$ (solid) and 9.91 (dotted) nm. The gate-controlled current densities are evaluated by integrating the transmission spectra at a bias voltage of 0 V over the energy regime of 0.5 eV with respect to the center energy of the integration region. The shift of the center energy can be assumed to be a back-gate voltage. The currents are normalized to the AGNR width of 0.76 nm. The eigenvalues for the AGNRs on both SiO_2/Si are shifted downward by 0.7 eV from those of the freestanding AGNR for comparison.

Figure 5(a) shows the current densities on linear scales. The current in the n side (electron current) for $L = 15.1$ nm is smaller than that for $L = 9.91$ nm for the freestanding AGNR, but we could not find any pronounced difference between the results for $L = 15.1$ and 9.91 nm for the AGNRs on both SiO_2/Si. The current in the p side (hole current) in the AGNRs on both SiO_2/Si is smaller than that in the freestanding AGNR. However, the current in the n side exhibits a steep rise for the AGNRs on both SiO_2/Si. Figure 5(b) shows the current densities on log scales. We define the on and off current densities as the maximum and minimum values among the calculated current densities, respectively. Since the on currents do not depend on the substrate environments and the channel length in an order of magnitude, the off currents dominate the on/off current ratios. For the freestanding AGNR, the off current densities exponentially decrease with respect to L and the ratio is 10^{21} and 10^{13} for $L = 15.1$ and 9.91 nm, respectively. For the AGNR on O-terminated SiO_2/Si, on the other hand, the off current densities are independent with the channel length L. The on/off current ratio is 10^5 for both L. Thus, we have found that the adjacent SiO_2/Si limits the on/off current ratio of AGNRs.

To understand the current densities, we show the transmission spectra obtained at a bias voltage of 0 V in Fig. 6. All the models have a transmission gap of 1.6 eV, which agrees with the energy band gap of AGNR with $N = 7$. The transmission gaps for AGNRs on both SiO_2/Si are shifted by 0.7 eV, regardless of L, indicating the p-type conduction of the AGNRs. On a linear scale [Fig. 6(a)], the transmission for the freestanding AGNR is increased from 2 to 6 at almost regular energy intervals, indicating the existence of quantum conductance. A depression of the transmission is observed just above 1 eV for $L = 15.1$ nm, resulting in the smaller electron current found in Fig. 5(a). We found that the depression

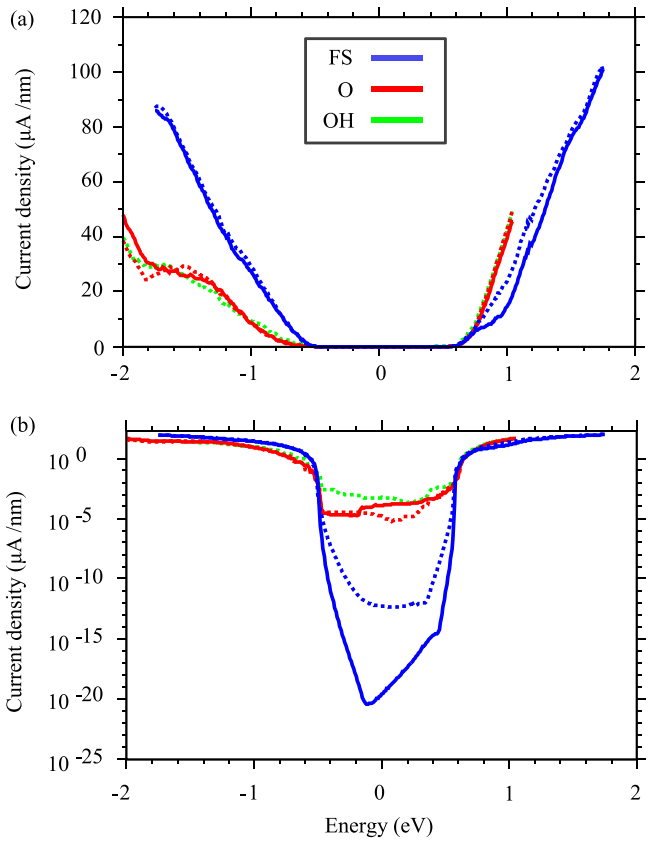

FIG. 5. Current densities on (a) linear and (b) log scales for the freestanding (FS) AGNR, and the AGNRs on O- and OH-terminated SiO_2/Si with channel lengths $L = 15.1$ (solid) and 9.91 (dotted) nm. There is no data for the AGNR on OH-terminated SiO_2/Si with $L = 15.1$ nm. The energy values for the AGNRs on O- and OH-terminated SiO_2/Si are shifted downward by 0.7 eV for comparison.

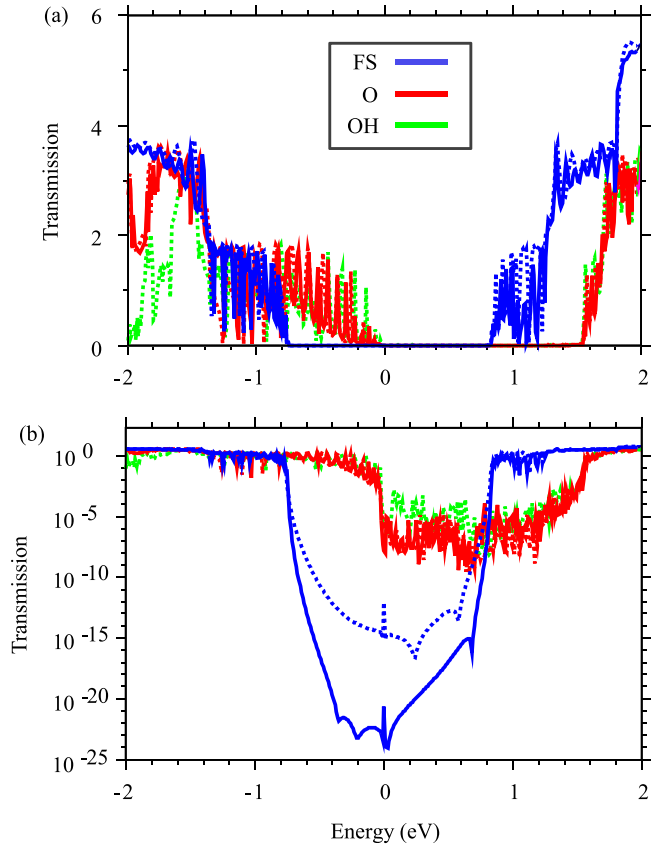

FIG. 6. Transmission spectra at a bias voltage of 0 V on (a) linear and (b) log scales for the freestanding (FS) AGNR, and the AGNRs on O- and OH-terminated SiO_2/Si with the channel lengths $L = 15.1$ (solid) and 9.91 (dotted) nm. There is no data for the AGNR on OH-terminated SiO_2/Si with $L = 15.1$ nm.

is caused by a mismatch in character between the channel and the lead electrodes and its energy is varied depending on the channel length. This phenomenon may be observed even for longer channel devices as long as we use thin leads. For the AGNRs on both SiO_2/Si, the energy regime with a transmission of about 2 is narrower on the *n* side (around 1.6 eV), leading to the steep increase in the electron current. Moreover, the transmission shows discrete peak structures on the *p* side (below 0 eV), decreasing the hole current. The energy interval of the discrete peaks is 0.07 and 0.11 eV for $L = 15.1$ and 9.91 nm, respectively. The interval is found to be inversely proportional to L, indicating the presence of Schottky barriers at the interface between the *p*-type semiconductor of the AGNR channel and the metallic AGNR leads.

On a log scale [Fig. 6(b)], we can see that the minimums of the transmission spectra within the gap are very large for the AGNRs on both SiO_2/Si compared with the freestanding AGNR. The minimum transmissions exponentially decrease with L for the freestanding AGNR, where the value is 10^{-24} and 10^{-16} for $L = 15.1$ and 9.91 nm, respectively. For the AGNR on O-terminated SiO_2/Si, however, the minimum transmissions are independent of L and the multiple spiky peaks are found in the transmission spectra within the gap.

We analyze the PDOS of each carbon atom in the AGNRs in Fig. 7. The lateral and vertical axes are the x axis in Fig. 4 and the energy relative to the Fermi level of the leads, respectively. For the freestanding AGNR [Fig. 7(a)], the PDOS tails extend from the left side along the x axis; however, there is a clear gap of 1.6 eV in the middle of the channel around zero energy, which corresponds well to the transmission gap. The transmission gap can be seen as the potential barrier to tunneling from the left lead to the right lead. The barrier height is independent of L; however, the range of the potential barrier depends on L. The minimum transmission exponentially decreases with increasing L for the freestanding AGNR. In contrast, for the AGNRs on O- and OH-terminated SiO_2/Si [Figs. 7(b) and 7(c)], the simple assumption of the tunneling barrier is inapplicable; multiple gap states are observed throughout the channel. These gap states may cause the spiky transmission peaks within the gap and disturb the exponential decay of the minimum transmission with respect to L. We also observe the Schottky barriers for the AGNRs on O- and OH-terminated SiO_2/Si. In real experiments, graphene is typically supported on the

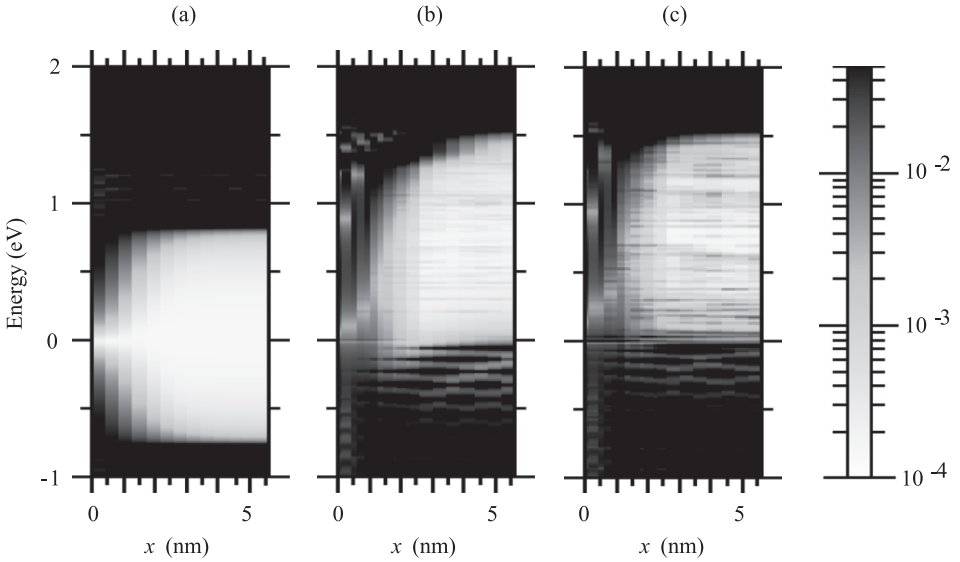

FIG. 7. PDOS profiles for each carbon atom in AGNRs for three models with the channel length $L = 9.91$ nm: (a) freestanding, (b) on O-terminated SiO_2/Si, and (c) on OH-terminated SiO_2/Si. The lateral axis indicates the x position of the carbon atoms shown in Fig. 4. The left lead extends from $x = 0$ to $x = 0.86$ nm. Only the left half region is shown because of the symmetry between the left and right half regions. The vertical axis is the energy relative to the Fermi level of the leads. The right color bar shows the PDOS value.

amorphous surface of SiO_2, where an electronic charge density displacement is promoted[39] and the dangling oxygen bonds show an additional ionic contribution.[40] These additional effects may degrade the transport properties further in the realistic devices.

We have found that the adjacent SiO_2/Si degrades the on/off current ratio of AGNRs and the ratio is independent with the channel length. The electrical transport experiments on sub-10 nm GNRs on SiO_2 have been performed with chemically derived GNRs with ultrasmooth edges.[20] The field effect transistor using GNRs with a width of 5 nm showed an on current of 2 μA and an on/off ratio of 10^5 at a channel length of 210 nm and a source-drain voltage of 0.5 V, which is the same value as the integration region in our current calculations. Although the GNR width is still wider than in our calculations, the on/off ratio is consistent with our results of 10^5 regardless of L on SiO_2/Si. The smaller on current in the experiment is mainly attributed to the contacts with the actual metal leads. The degradation of the on/off ratio by the adjacent SiO_2/Si was also directly or experimentally observed by using the suspended (freestanding) GNR channels.[19] For example, the freestanding GNRs exhibit the ratio of 10^4, while GNRs on SiO_2 have the ratio of 10^1 at a ribbon width of 20 nm and a source-drain voltage of 0.5 V.[20]

In our calculations, the AGNRs on SiO_2/Si show the *p*-type conduction, whereas no doping effect was found on graphene using the fully O-terminated SiO_2 slab models.[24,25] The hole doping of the graphene may be ascribed to the very thin SiO_2 layer in our model. The O-terminated SiO_2/Si model shows an electron affinity level of 4.8 eV (cf. that of 0.9 eV for bulk SiO_2), which is deeper than the work function of 4.2 eV for graphene.

C. SiO_2 termination dependence of transport properties

In this section, we present the supplemental results about the dependence of the transport properties on the surface termination of SiO_2, which were discussed in Ref. 26. As shown in Figs. 5 and 6, the transmission in the *p* side of the gap for the OH-terminated surface is larger than that for the O-terminated one, resulting in the degradation of the on/off current ratio. Figure S6 in the supplementary material shows the PDOS of a carbon atom in the AGNR and a topmost oxygen atom in the SiO_2/Si surface. We observe several PDOS peaks in the energy gap AGNRs on both the SiO_2 surfaces in Figs. S6(b) and S6(c). They correspond to the gap states in Figs. 7(b) and 7(c). In contrast, no peaks are observed in the gap for the freestanding AGNR in Fig. S6(a). Energy positions of the peaks for the carbon atom correlate with those of the oxygen atom, indicating a substantial interaction between the AGNRs and the SiO_2/Si surfaces despite the large spacing of about 0.3 nm. We also find large peaks around −0.5 eV and above 0 eV in the PDOS of the oxygen atom in the OH groups; however, these peaks are not observed for the oxygen atom of the O-terminated surface. These two peaks can be interpreted as the bonding and antibonding states originating from the interaction between the localized states around the OH groups (Fig. S7 in the supplementary material) and the AGNRs. The peak above the Fermi energy explains the larger transmission in the *p* side of the gap for the AGNR on OH-terminated SiO_2/Si.

V. SUMMARY

The one-atom thickness of graphene is one of the greatest advantages in using it in 10 nm-scale devices. However, it simultaneously leads to problems arising from the fragility of the transport properties of graphene against other foreign materials such as metal electrodes and insulating substrates. In this paper, we studied the electronic transport properties of AGNRs bridged between the two metal electrodes and supported on SiO_2/Si substrates in 10 nm-scale devices using the first-principles calculations.

We investigated the electronic transport properties of the hybrid structures of graphene/metal electrodes. The models consist of AGNRs with the ribbon width of about 12 nm bridged between the two metal electrodes of Ti(0001) and Au(111). The results show that the current densities for the Ti electrodes are about 10 times as large as those for the Au electrodes. For the Ti electrodes, the strong π-*d* hybridization modifies the electronic structure of the graphene and substantially enhances the transmission through the graphene-Ti contact. For the Au electrodes, the energy band structure and the symmetry of π states of graphene play an important role in determining the transport properties because of the weak interaction between the π states of graphene and the *s* states of the Au surface. We have found that the transport properties of the hybrid structures of graphene/metal electrodes decisively depend on the amount of hybridization between them. It is important to choose the metal species even for the 10 nm-scale graphene devices.

We also investigated the electronic transport properties of AGNRs with $N = 7$ on O- and OH-terminated SiO_2/Si substrates. We consider two AGNRs with two different channel lengths of 15.1 and 9.91 nm for the AGNR on O-terminated SiO_2/Si. The off current for the AGNR on O-terminated SiO_2/Si is independent of the channel length due to the PDOS peaks within the band gap, although it decreases exponentially when increasing the channel length for the freestanding AGNR. The off current is even larger on the *p* side for the OH-terminated SiO_2. Thus, we have found that the gap states originating from the interaction between the AGNR and the SiO_2/Si surface limit the off currents, regardless of the channel length. We can conclude that it is essentially difficult to obtain a large on/off current ratio for the AGNRs on the SiO_2/Si surfaces.

In this paper, we assume that the perfect GNRs are adsorbed on clean crystalline metal and insulator surfaces. However, actual interface of them generally has a lot of impurities such as water, oxygen, and organic materials from the resist residuals. There are also structural imperfections such as the deformation and the defect in the graphene and the non-crystalline substrate. They can disturb the orbital hybridization and change the energy shift by the doping between the graphene and the surrounding materials, which are important factors on the transport properties

of the graphene devices especially in the 10-nm scale. To obtain further theoretical insight for realizing the graphene devices, we should perform the calculations considering the effects of the impurities and the structural imperfections on the transport properties. For such calculations, the results of this study will be useful as a reference data of an ideal interface model. We have separately studied the effects on the transport properties of the metal electrodes and the insulating substrates due to the limit of the computational costs. In the future, we would like to explore more realistic models including both the metal electrodes and the insulating substrates by improving the code for the larger-scale calculations.

SUPPLEMENTARY MATERIAL

See the supplementary material for Figs. S1–S7.

ACKNOWLEDGMENTS

We thank Dr. T. Yamasaki (National Institute for Materials Science) for offering the geometric data and discussing about the SiO_2/Si model. The calculations were performed on the Fujitsu FX10 supercomputer system of the University of Tokyo and the Cray XC30 supercomputer system of the Japan Advanced Institute of Science and Technology. This work was supported by Priority Issue (creation of new functional devices and high-performance materials to support next-generation industries) to be tackled by using Post "K" Computer, MEXT, Japan.

[1]K. Nagashio, T. Nishimura, K. Kita, and A. Toriumi, Appl. Phys. Lett. **97**, 143514 (2010).
[2]J. A. Robinson, M. Labella, M. Zhu, M. Hollander, R. Kasarda, Z. Hughes, K. Trumbull, R. Cavalero, and D. Snyder, Appl. Phys. Lett. **98**, 53103 (2011).
[3]R. Nouchi, T. Saito, and K. Tanigaki, J. Appl. Phys. **111**, 84314 (2012).
[4]R. Ifuku, K. Nagashio, T. Nishimura, and A. Toriumi, Appl. Phys. Lett. **103**, 33514 (2013).
[5]M. Politou, I. Asselberghs, I. Radu, T. Conard, O. Richard, C. S. Lee, K. Martens, S. Sayan, C. Huyghebaert, Z. Tokei, S. De Gendt, M. Heyns, M. Politou, I. Asselberghs, I. Radu, T. Conard, O. Richard, C. S. Lee, K. Martens, S. Sayan, C. Huyghebaert, and Z. Tokei, Appl. Phys. Lett. **107**, 153104 (2015).
[6]E. Watanabe, A. Conwill, D. Tsuya, and Y. Koide, Diamond Relat. Mater. **24**, 171 (2012).
[7]P. A. Khomyakov, G. Giovannetti, P. C. Rusu, G. Brocks, J. Van Den Brink, and P. J. Kelly, Phys. Rev. B **79**, 195425 (2009).
[8]Q. Ran, M. Gao, X. Guan, Y. Wang, and Z. Yu, Appl. Phys. Lett. **94**, 103511 (2009).
[9]C. Gong, G. Lee, B. Shan, E. M. Vogel, R. M. Wallace, and K. Cho, J. Appl. Phys. **108**, 123711 (2010).
[10]Y. Takagi and S. Okada, Jpn. J. Appl. Phys., Part 1 **51**, 85102 (2012).
[11]K. Stokbro, M. Engelund, and A. Blom, Phys. Rev. B **85**, 165442 (2012).
[12]H. Liu, H. Kondo, and T. Ohno, Phys. Rev. B **86**, 155434 (2012).
[13]H. Liu, H. Kondo, and T. Ohno, J. Chem. Phys. **139**, 74703 (2013).
[14]H. Jippo, M. Ohfuchi, and S. Okada, e-J. Surf. Sci. Nanotechnol. **13**, 54 (2015).
[15]K. S. Novoselov, A. K. Geim, S. V. Morozov, D. Jiang, Y. Zhang, S. V. Dubonos, I. V. Grigorieva, and A. A. Firsov, Science **306**, 666 (2004).
[16]K. I. Bolotin, K. J. Sikes, Z. Jiang, M. Klima, G. Fudenberg, J. Hone, P. Kim, and H. L. Stormer, Solid State Commun. **146**, 351 (2008).
[17]X. Du, I. Skachko, A. Barker, and E. Y. Andrei, Nat. Nanotechnol. **3**, 491 (2008).
[18]K. Nagashio and T. Yamashita, J. Appl. Phys. **110**, 24513 (2011).
[19]M.-W. Lin, C. Ling, Y. Zhang, H. J. Yoon, M. M.-C. Cheng, L. A. Agapito, N. Kioussis, N. Widjaja, and Z. Zhou, Nanotechnology **22**, 265201 (2011).
[20]X. Li, X. Wang, L. Zhang, S. Lee, and H. Dai, Science **319**, 1229 (2008).
[21]Y.-J. Kang, J. Kang, and K. J. Chang, Phys. Rev. B **78**, 115404 (2008).
[22]M. Z. Hossain, Appl. Phys. Lett. **95**, 143125 (2009).
[23]P. Shemella and S. K. Nayak, Appl. Phys. Lett. **94**, 32101 (2009).
[24]N. T. Cuong, M. Otani, and S. Okada, Phys. Rev. Lett. **106**, 106801 (2011).
[25]C.-J. Yang, S.-J. Huang, and C.-L. Kuo, Appl. Phys. Lett. **101**, 253107 (2012).
[26]H. Jippo, T. Ozaki, and M. Ohfuchi, Appl. Phys. Express **7**, 25101 (2014).
[27]L. T. Zhuravlev, Colloids Surf., A **173**, 1 (2000).
[28]T. Ozaki, Phys. Rev. B **67**, 155108 (2003).
[29]T. Ozaki, K. Nishio, and H. Kino, Phys. Rev. B **81**, 35116 (2010).
[30]T. V. T. Duy and T. Ozaki, Comput. Phys. Commun. **185**, 153 (2014).
[31]T. V. T. Duy and T. Ozaki, Comput. Phys. Commun. **185**, 777 (2014).
[32]J. P. Perdew, K. Burke, and M. Ernzerhof, Phys. Rev. Lett. **77**, 3865 (1996).
[33]I. Morrison, D. M. Bylander, and L. Kleinman, Phys. Rev. B **47**, 6728 (1993).
[34]S. G. Louie, S. Froyen, and M. L. Cohen, Phys. Rev. B **26**, 1738 (1982).
[35]T. Ozaki, Phys. Rev. B **74**, 245101 (2006).
[36]H. Jippo and M. Ohfuchi, J. Appl. Phys. **113**, 183715 (2013).
[37]Y. Lu and J. Guo, Nano Res. **3**, 189 (2010).
[38]T. Yamasaki, K. Kato, and T. Uda, Phys. Rev. Lett. **91**, 146102 (2003).
[39]R. H. Miwa, T. M. Schmidt, W. L. Scopel, and A. Fazzio, Appl. Phys. Lett. **99**, 163108 (2011).
[40]A. N. Rudenko, F. J. Keil, M. I. Katsnelson, and A. I. Lichtenstein, Phys. Rev. B **84**, 85438 (2011).